

Continuum simulations of water flow in carbon nanotube membranes

This content has been downloaded from IOPscience. Please scroll down to see the full text.

2014 New J. Phys. 16 082001

(<http://iopscience.iop.org/1367-2630/16/8/082001>)

View [the table of contents for this issue](#), or go to the [journal homepage](#) for more

Download details:

IP Address: 193.2.10.161

This content was downloaded on 04/08/2014 at 09:10

Please note that [terms and conditions apply](#).

Fast Track Communication

Continuum simulations of water flow in carbon nanotube membranes

A Popadić¹, J H Walther^{2,3}, P Koumoutsakos³ and M Praprotnik¹

¹Laboratory for Molecular Modeling, National Institute of Chemistry, Hajdrihova 19, SI-1001 Ljubljana, Slovenia

²Department of Mechanical Engineering, Technical University of Denmark, DK-2800 Kgs. Lyngby, Denmark

³Chair of Computational Science, ETH Zurich, Clausiusstrasse 33, CH-8092 Zurich, Switzerland

E-mail: jhw@mek.dtu.dk, petros@ethz.ch and praprot@cmm.ki.si

Received 21 May 2014, revised 5 July 2014

Accepted for publication 15 July 2014

Published 4 August 2014

New Journal of Physics **16** (2014) 082001

[doi:10.1088/1367-2630/16/8/082001](https://doi.org/10.1088/1367-2630/16/8/082001)

Abstract

We propose the use of the Navier–Stokes equations subject to partial-slip boundary conditions to simulate water flows in Carbon NanoTube (CNT) membranes. The finite volume discretizations of the Navier–Stokes equations are combined with slip lengths extracted from molecular dynamics (MD) simulations to predict the pressure losses at the CNT entrance as well as the enhancement of the flow rate in the CNT. The flow quantities calculated from the present hybrid approach are in excellent agreement with pure MD results while they are obtained at a fraction of the computational cost. The method enables simulations of system sizes and times well beyond the present capabilities of MD simulations. Our simulations provide an asymptotic flow rate enhancement and indicate that the pressure losses at the CNT ends can be reduced by reducing their curvature. More importantly, our results suggest that flows at nanoscale channels can be described by continuum solvers with proper boundary conditions that reflect the molecular interactions of the liquid with the walls of the nanochannel.



Content from this work may be used under the terms of the [Creative Commons Attribution 3.0 licence](https://creativecommons.org/licenses/by/3.0/). Any further distribution of this work must maintain attribution to the author(s) and the title of the work, journal citation and DOI.

 Online supplementary data available from stacks.iop.org/njp/16/082001/mmedia

Keywords: carbon nanotube membrane, computational fluid dynamics, partial-slip boundary condition

1. Introduction

In recent years, detailed experiments and simulations have demonstrated that flows in natural and artificial nanochannels exhibit remarkably high flow rates [1–6]. These findings have spurred great interest in applications ranging from nanosyringes for drug delivery to new technologies for water desalination [7, 8].

The two main lines of investigation for these flows involve experiments and simulations using molecular dynamics (MD). These two approaches are considered complementary, however, there are large discrepancies in the spatiotemporal scales that each can resolve. These discrepancies have fueled arguments with regards to the large differences observed in flow enhancement rates calculated in experiments and MD simulations [4, 9, 10].

The computational cost of the MD simulations and the relatively short time scales that they resolve has motivated the development of a continuum model [11] with partial-slip boundary conditions to model fluid flows through carbon nanotube (CNT) membranes. Such partial slip boundary conditions are consistent with the observation that at the nanoscale the wall-fluid interaction plays an important role on the overall behavior of the flow and the standard empirical law of the no-slip boundary condition is not applicable [12].

2. Governing equations

In this work, we present a continuum, numerical study of water flow through CNT membranes using finite volume discretization of the steady-state incompressible Navier–Stokes equations:

$$\text{Re} \left(\mathbf{v}^* \cdot \nabla \right) \mathbf{v}^* = -\nabla p^* + \nabla^2 \mathbf{v}^*, \quad \nabla \cdot \mathbf{v}^* = 0, \quad (1)$$

subject to partial-slip boundary condition at the fluid-wall interface:

$$v_t = l_s \left[\frac{\partial v_t}{\partial n} - \frac{v_t}{r} \right], \quad (2)$$

where v_t is the tangential to the wall component of the fluid velocity and $\partial v_t / \partial n$ its gradient in the direction normal to the wall [13], r is the radius of the curvature of the wall in the flow direction with the radius being negative for concave boundaries and l_s is the slip length. The slip length is defined as the ratio between the fluid viscosity and the friction coefficient between the wall and the fluid and can be extracted from MD simulations [9, 14–16]. The derivation of the partial-slip boundary condition is given in the supplementary material, available from stacks.iop.org/njp/16/082001/mmedia.

The equations are written in non-dimensional form, where $\mathbf{v}^* \equiv \mathbf{v}/U$ and $p^* = pR/(\mu U)$ are the non-dimensional fluid velocity and pressure, respectively. ρ is the fluid density, and U

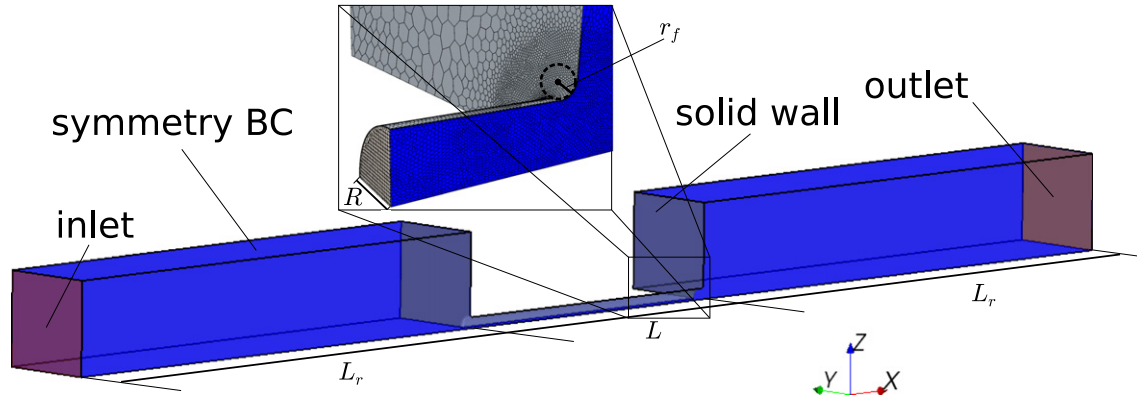


Figure 1. The geometry of the computational system. The computational domain is reduced to a quarter due to the symmetry of the problem. The CNT of radius R and length L is connecting two large water reservoirs of length L_r . The edges at the CNT ends are rounded with a fillet of constant curvature r_f (see insert). We apply the partial-slip boundary conditions to the solid walls of the membrane and CNT surfaces. The origin of the coordinate system is placed in the center of the CNT and the x axis points in the direction of the flow.

the characteristic velocity of the flow through the CNT. The Reynolds number is $Re = \rho UR/\mu$, where μ the fluid viscosity, and R the radius of the CNT.

3. Methodology

The CNT membrane is modeled as a collection of circular pipes connecting two water reservoirs. The radius $R = 1.017$ nm is identical to the CNT membrane used in the recent MD study of Walther *et al* [4]. The length (L) of the CNT varies between 3 and 7000 nm. The CNT membrane is set up so that the CNTs form a rectangular lattice with the displacements between adjacent CNTs of 18.17 nm in one direction and 17.87 nm in the other direction. Using the symmetries of the CNT membrane we reduce the computational domain to a quarter of a single CNT (see figure 1). On either side of the CNT we place a reservoir extending 50 nm away from the CNT membrane. At the inlet side of the reservoir we apply a uniform velocity boundary condition maintaining a constant volumetric flow in the range of $0.8 \mu\text{m}^3 \text{s}^{-1}$ – $10 \mu\text{m}^3 \text{s}^{-1}$ through a single CNT. At the outlet we impose a uniform pressure boundary condition and the CNT entrance and exit have edges with a radius of curvature (r_f) ranging from 0.0 nm to 0.6 nm. Unless otherwise stated we consider sharp edges (the radius of curvature of the fillet is 0 nm). We use $\mu = 7.2 \times 10^{-4} \text{ kg ms}^{-1}$ and $\rho = 997 \text{ kg m}^{-3}$ for water viscosity and density, respectively, corresponding to the SPC/E water model at ambient conditions [17, 18]. Here the Reynolds number is $Re = \mathcal{O}(10^{-3})$. The incompressible Navier–Stokes equation (1) are solved using a second order finite volume method. The flow is assumed steady and we use the SIMPLE algorithm [19] implemented in the STAR-CD simulation package, into which we implemented the partial-slip boundary conditions [20].

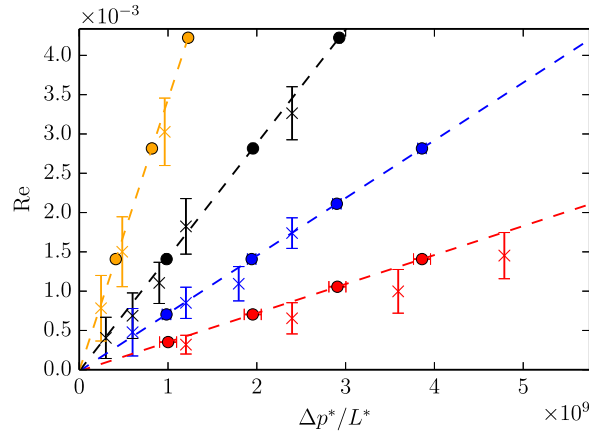


Figure 2. Comparison of MD data with CFD simulations. For the slip length we use $l_s = 63$ nm ($l_s^* = 62$), a value obtained in the recent MD study [4]. The figure shows pressure gradient along the CNT dependence from the Reynolds number. Crosses represent the MD results and circles the CFD results. Dashed lines serve as a visual guide and are fits of a linear equation to the CFD results. Orange color represents the results for a nanotube of length 30 nm, black for 12 nm, blue for 6 nm and red for 3 nm.

4. Results

We verify the accuracy of the partial-slip model by comparing the present continuum results with those obtained by related MD simulations [4] cf figure 2. We use $l_s = 63$ nm ($l_s^* \equiv l_s/R = 62$) obtained in this recent study. Our results on flow rates are within the error bars of the values obtained with MD simulations. We note that recently it has been reported [21, 22] that in highly confined nanoscale channels an extended Navier–Stokes equation coupled to the microscopic molecular spin angular velocity describes the water flow better than the standard Navier–Stokes equation. According to our results the standard Navier–Stokes equation still gives the correct description of flow in highly confined channels when the slip length is large. Large slip lengths, corresponding to hydrophobic walls, decrease the effect of the coupling of the Navier–Stokes equation to the microscopic molecular spin angular velocity. Our slip-length $l_s = 63$ nm is more than an order of magnitude larger than the slip length in Hansen *et al* [21].

The introduction of the partial-slip boundary condition has a significant effect on the pressure profile along the CNT and the water flow through the CNT. Figure 3 shows the pressure loss between the inlet and the outlet dependence on the slip length. The figure shows the results from our simulations as well as the results predicted by the model proposed by Sisan and Lichter [11]

$$\Delta p^* = \frac{8L^*}{1 + 4l_s^*} + \pi C, \quad (3)$$

where $C = 3$, Δp^* is the non-dimensional pressure loss between the inlet and the outlet and $L^* = L/R$ is the non-dimensional CNT length. The above equation attributes the overall pressure loss along the CNT to two contributions: pressure loss due to a fully developed flow inside the CNT given by the slip enhanced Hagen–Poiseuille equation and pressure loss at the CNT ends approximated by the pressure loss through a thin orifice [23, 24]. It is interesting to observe from figure 3 and equation (3) that even in the limiting case of full-slip ($l_s^* \rightarrow \infty$) the

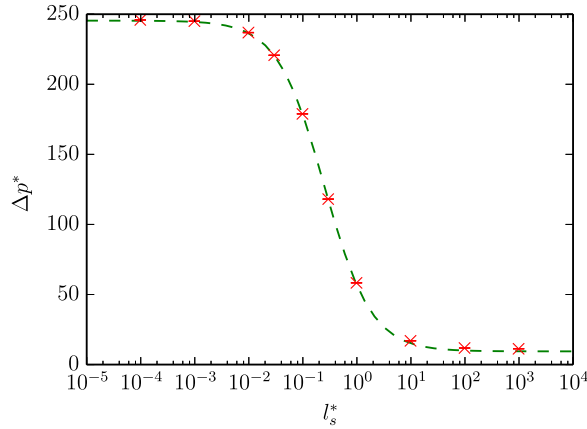


Figure 3. Pressure loss between the inlet and the outlet dependence from slip length along a CNT of length $L^* = L/R = 29.5$ with the Reynolds number $Re = 1.4 \times 10^{-3}$. The red X symbols represent pressure loss obtained by CFD simulations and the green dashed line represents pressure loss obtained from equation (3). Our error estimate due to discretization is roughly 0.2.

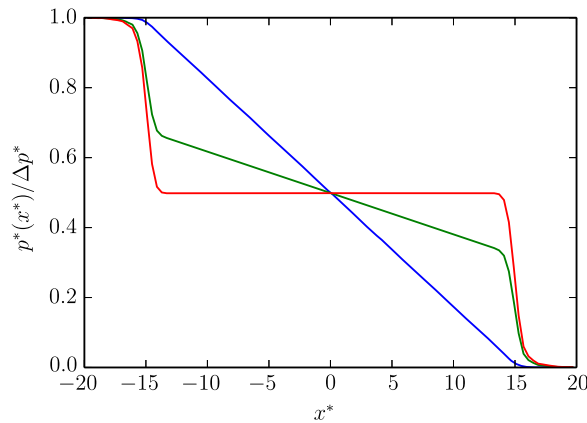


Figure 4. Pressure profile along the axis of a CNT of length $L^* = 29.5$ with the Reynolds number $Re = 1.4 \times 10^{-3}$. The y axis shows the pressure profile normalized by the average pressure at the inlet. The three curves show the pressure profile for three different slip lengths at the fluid-wall interface. Blue line represents the pressure profile for no-slip ($l_s^* = 0$), green for partial-slip with $l_s^* = 10$ and red for full-slip ($l_s^* \rightarrow \infty$) case. Our error estimate due to discretization is roughly 0.001 for the no-slip and 0.01 for the partial-slip and full-slip cases.

pressure loss does not vanish [11, 25]. Figure 4 shows the pressure profile along the axis of the CNT. We observe that in the case of the standard no-slip boundary condition the pressure steadily drops through the CNT. In the case of the full slip boundary condition the pressure loss occurs solely at the CNT ends. For the partial-slip boundary condition pressure loss occurs both at the CNT ends and along the length of the CNT. The pressure loss at the CNT ends is present in the no-slip case as well. It is, however, negligible in comparison to the pressure loss inside the CNT. In the case of a large slip on the other hand the pressure loss at the CNT ends plays a significant role. We note from figure 3 that in the no-slip case the non-dimensional pressure loss

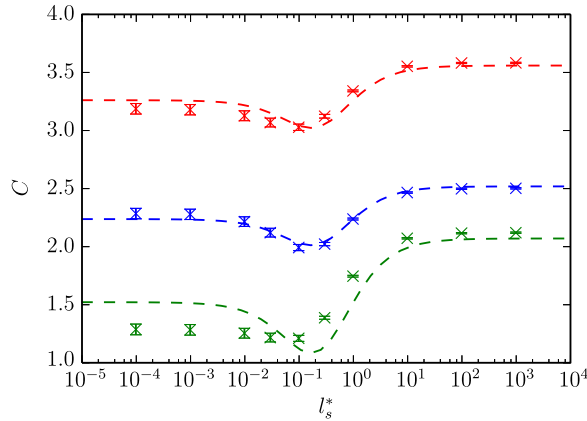


Figure 5. Pressure loss at the CNT ends dependence on l_s^* for different r_f^* : 0.0 (red), 0.3 (blue), 0.6 (green). The results are obtained for the Reynolds number $Re = 1.4 \times 10^{-3}$. The dashed curves represent fits of our model for pressure loss at CNT ends from equation (10) to the CFD results.

is approximately 250 and in the full-slip case about 10. Because of large slip effects in CNT membranes we study in detail the pressure loss at the CNT ends [26, 27]. The pressure loss at the CNT ends occurs due to viscosity, where a non-zero viscous part of the stress tensor can be significant at this low Reynolds number flow [28]. In the case without the partial-slip boundary condition the pressure loss at CNT ends could be estimated by dimensional analysis up to a multiplicative factor C [25],

$$\Delta p^* = \pi C. \quad (4)$$

This result is in agreement to the one obtained by Weissberg [29], who studied pressure losses at tube ends analytically and obtained an upper bound for the constant, $C \leq 3.47$. A similar expression was obtained by Samson [23] and Roscoe [24] for the pressure loss through a thin orifice, effectively a tube with a vanishing length. In this case the pressure loss is known exactly and the constant $C = 3$.

The partial-slip boundary condition introduces a new length scale into the problem (l_s^*) that characterizes the pressure loss at CNT ends. To this end, we measure the pressure loss at CNT ends dependence on the slip length. We adopt the same expression for the pressure loss as suggested by Sisan and Lichter [11] (equation (3)) with the difference that we view C as a function of l_s^* and r_f^* . The flow upon entering the CNT fully develops into the slip enhanced Hagen–Poiseuille flow within the length of the order of the CNT radius [11]. The pressure loss due to the CNT ends is therefore confined to their vicinity. We evaluate the pressure loss due to the CNT ends by calculating the pressure loss dependence of the CNT length. We estimate C by fitting equation (3) to the obtained results. We do this for varying l_s^* to obtain $C = C(l_s^*)$ and the results are shown in figure 5. The pressure loss at CNT ends clearly exhibits a dependence on l_s^* . Furthermore the transition of the pressure loss from the no-slip case to the full-slip case is not monotonous. Around $l_s^* \sim 0.1$ we observe a local minimum for the pressure loss at the CNT ends and the range of C is roughly between 3.0 and 3.6. In the large slip scenario, where the majority of the pressure loss along the CNT stems from the CNT ends, an accurate description of pressure loss at the CNT ends is vital and the choice of $C = 3$ might not be adequate. For $l_s^* \gg 1$ we observe C to be at its maximum. For $l_s^* = 1000$ we measure $C = 3.583 \pm 0.005$. Gravelle *et al* [5] in contrast give $C = 3.75$ for full-slip

case ($l_s^* \rightarrow \infty$). Gravelle *et al* also show that as the length of a tube approaches zero, C approaches 3. This is in agreement with analytical derivations for pressure loss through a thin orifice [23, 24]. For small slip $l_s^* = 10^{-4}$ on the other hand we measure $C = 3.19 \pm 0.05$, which is in agreement to Weissbergs $C \leq 3.47$. We explain the dependence of pressure loss at the CNT ends on l_s^* by considering the energy dissipation rate [28]

$$\dot{\mathcal{E}}^* = -\frac{1}{2} \int \left(\frac{\partial v_i^*}{\partial x_k^*} + \frac{\partial v_k^*}{\partial x_i^*} \right)^2 dV^*. \quad (5)$$

We divide the energy dissipation into two contributions: $\dot{\mathcal{E}}^* = \dot{\mathcal{E}}_1^* + \dot{\mathcal{E}}_2^*$ corresponding to the energy loss outside ($\dot{\mathcal{E}}_1^*$) and inside ($\dot{\mathcal{E}}_2^*$) of the CNT, respectively. We assume a sharp edge at the CNT ends (i.e. $r_f^* = 0$ at the CNT ends). The sharp edges at the CNT ends imposes an effective no-slip boundary condition at the point of the corner. We assume that the velocity profile at the CNT end is independent from l_s^* and is equal to the velocity profile of the fluid flow through a thin orifice [29]

$$v_0^*(r^*) = \frac{3}{2} \sqrt{1 - r^{*2}}. \quad (6)$$

The pressure loss outside the CNT is then equal to the pressure loss for a flow through a thin orifice and is given by equation (4) where $C = C_1 = 3$ (corresponding to $\dot{\mathcal{E}}_1^* = \pi^2 C_1$). Inside the CNT we restrict ourselves only to the axial component of the velocity. The pressure loss due to dependence of the velocity from the radial coordinate is included in the slip enhanced Hagen–Poiseuille equation (first term in equation (3)) although in the vicinity of the CNT ends not completely accurate. We thus restrict ourselves to the velocity dependence from the axial coordinate. We assume a linear transition from the velocity profile in equation (6) to the velocity profile of the fully developed slip enhanced Hagen–Poiseuille flow

$$v^*(r^*) = 2 \frac{1 + 2l_s^* - r^{*2}}{1 + 4l_s^*}, \quad (7)$$

and we assume that the transition happens in the length proportional to the CNT radius. Energy dissipation is then approximated by

$$\dot{\mathcal{E}}_2^* \propto \int_0^1 (v^* - v_0^*)^2 r^* dr^*, \quad (8)$$

Upon integrating, and considering $\dot{\mathcal{E}}^* = \pi \Delta p^*$, we obtain

$$\Delta p_2^* \propto \pi \frac{240l_s^{*2} - 72l_s^* + 7}{(1 + 4l_s^*)^2}. \quad (9)$$

Pressure loss due to CNT ends is thus given by

$$\Delta p = \pi \left(C_1 + C_2 \frac{240l_s^{*2} - 72l_s^* + 7}{(1 + 4l_s^*)^2} \right), \quad (10)$$

where $C_1 = 3$. By fitting the above expression to the CFD results we obtain $C_2 = 0.038 \pm 0.002$ (figure 5). The model described above gives a minimum pressure loss at the CNT ends for $l_s^* = 1/6$. At this l_s^* the velocity profile at the CNT ends (equation (6)) bears the closest resemblance to the fully developed slip enhanced Hagen–Poiseuille flow (equation (7)). This results in the least dissipated energy during the development of the flow. We also check the effect of slip at the outer walls of the CNT membrane (see supplementary material). We test three cases. One where there is no slippage present at the outer walls, one with full-slip at the outer walls and one where the boundary condition at the outer walls is equal to the boundary condition at the CNT wall. The results show that slip at the outer walls has a negligible effect on the pressure loss. This is in agreement to Gravelle *et al* [5] who also found the boundary condition at the outer walls to have negligible impact.

The pressure loss at the CNT ends is due to viscous dissipation of energy. In the vicinity of the CNT openings the streamlines sharply curve into and out of the CNT. This results in a non-vanishing viscous part of the stress tensor and consequentially viscous energy dissipation. This kind of viscous energy dissipation can be reduced by softening the streamline curvature. We therefore test the effect of softer corners at the CNT ends. We round the corners by introducing a fillet of constant curvature $r_f^* \equiv r_f/R$. This introduces yet another length scale and we now view the constant C as a function of two variables: the slip length (l_s^*), and the curvature radius of the fillet (r_f^*). We measure the dependence of the constant C on the slip length as shown in figure 5. We also test our model for pressure loss at the CNT ends. The assumptions we made when developing the model are not valid any more due to the rounded corners. Therefore, we do not fit equation (10) only for C_2 but also for C_1 . We obtain $C_1 = 1.99 \pm 0.02$ and $C_2 = 0.036 \pm 0.002$ for $r_f^* = 0.3$, and $C_1 = 1.0 \pm 0.1$ and $C_2 = 0.07 \pm 0.01$ for $r_f^* = 0.6$. The results shown in figure 5 confirm that our model is able to describe the pressure loss at the CNT ends correctly for rounded corners with small curvature radius $r_f^* \leq 0.3$. However, it breaks at larger curvature radius where our assumptions (equation (6)) upon which we developed the model are no longer valid. We find that the rounded corners at the CNT ends reduce the energy dissipation. Figure 6 shows energy dissipation rates per unit volume for three different boundary conditions: the full-slip boundary condition, the partial-slip boundary condition with $l_s^* = 1/6$ and the no-slip boundary condition. For the full-slip case the energy dissipation rate is highest near the corner at the CNT entrance. For the no-slip case on the other hand it is highest near the walls of the CNT. For the partial slip case with $l_s^* = 1/6$ it is comparable in both regions. We also observe high pressure gradients at the wall near the transitions from the rounded corner to the outer membrane wall and the inner CNT wall cf figure 6. The high pressure gradients can be understood by considering the partial-slip boundary condition cf equation (2) and recognizing that the shear stress at the wall is linearly proportional to the flow velocity at the wall (see supplementary material). At the transition from the rounded corner to the straight wall the radius of curvature changes discontinuously from r_f^* to ∞ corresponding to the curvature radius of a straight wall. The discontinuous curvature results in a discontinuous wall shear stress and surface pressure gradient. The flow velocity is higher at the fillet-CNT connection than it is at the fillet-outer membrane wall connection with correspondingly higher pressure gradient at the fillet-CNT transition than at the fillet-outer membrane wall transition. In the limiting case of no-slip ($l_s^* = 0$), however, the flow velocity at the wall is zero which results in a vanishing curvature term (equation (2)) and hence a continuous stress at the wall. Indeed, the pressure gradient is significantly smaller for the system with no-slip boundary condition than for the system with full or partial slip.

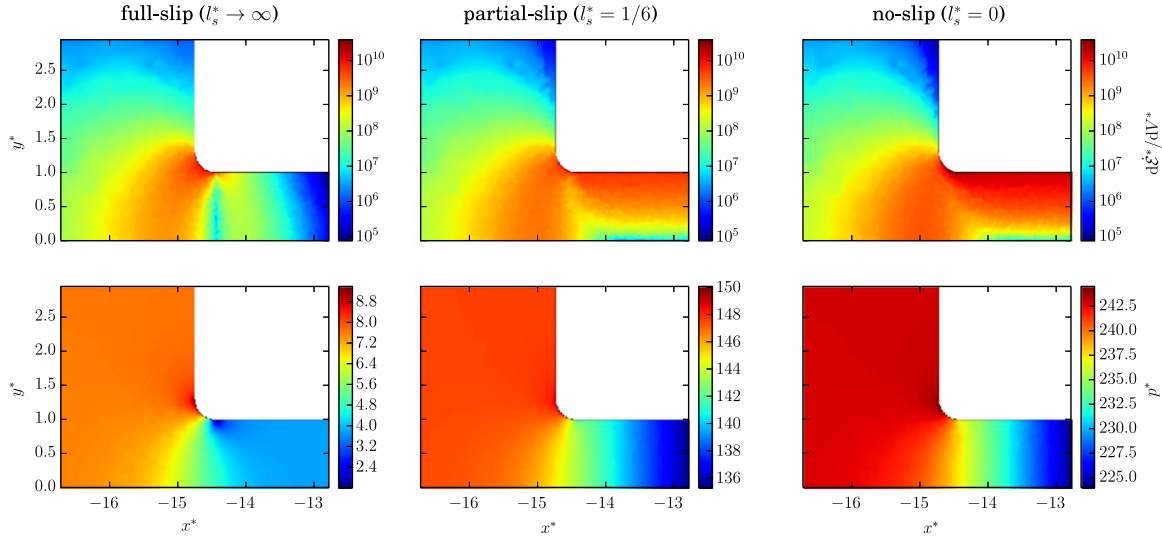


Figure 6. Energy dissipation rate per unit volume (top) and pressure profile (bottom) in the vicinity of the CNT entrance with a rounded corner by a fillet with the radius of curvature of $r_f^* = 0.3$. The Reynolds number is $Re = 1.4 \times 10^{-3}$. (left) Full-slip boundary condition ($l_s^* \rightarrow \infty$). (middle) Partial-slip boundary condition ($l_s^* = 1/6$). (right) No-slip boundary condition ($l_s^* = 0$). For full-slip boundary condition the energy dissipation rate is highest near the corner at the CNT entrance whereas it is highest near the walls of the CNT for the no-slip boundary condition. For the partial-slip boundary condition with $l_s^* = 1/6$, however, the energy dissipation is comparable at the CNT entrance and the walls of the CNT ends. High pressure gradients are visible at the rounded corner edges, where the curvature changes discontinuously from the curvature of the fillet ($r_f^* = 0.3$) to the curvature of the straight wall ($r \rightarrow \infty$).

Finally, we perform simulations of CNT membranes with lengths varying from 3 nm to 7000 nm exceeding the current state-of-the art MD simulations [4] at a fraction of the computational cost. We measure the flow rate enhancement (E) as the ratio of the flow rate ($Q^* = \pi$) predicted using the continuum model to the corresponding no-slip Hagen–Poiseuille value $Q_{HP}^* = \pi \Delta p^* / (8L^*)$

$$E = \frac{Q^*}{Q_{HP}^*}. \quad (11)$$

Combining equations (3) and (11) we obtain

$$E = \left(\frac{1}{1 + 4l_s^*} + \frac{C\pi}{8L^*} \right)^{-1}. \quad (12)$$

We maintain a constant Reynolds number $Re = 1.4 \times 10^{-3}$ in the CFD simulations and apply the partial-slip boundary condition with $l_s^* = 62$ and $C = 3.6$ corresponding to the values predicted by the MD simulations [4]. The results are depicted in figure 7 and confirm that the enhancement is a function of the CNT length and reach an asymptotic value of 248 for $L > 2000$ nm. The present continuum model confirms the asymptotic value by allowing CNT lengths of 7000 nm, beyond the present capabilities of MD simulations. The measurement of the flow rate enhancement Q using CFD simulations for $L > 2000$ nm is enabled by the slip length

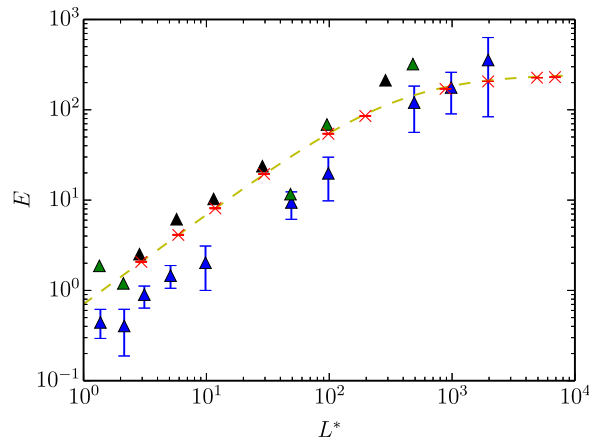


Figure 7. Flow rate enhancement (equation (11)) dependence from CNT length. The red X symbols show the flow rate enhancement for present study. The Reynolds number is $Re = 1.4 \times 10^{-3}$ and $l_s^* = 62$. The triangles show the flow rate enhancement for a recent MD study of water flow through CNT membranes [4]. The black triangles correspond to MD simulations using FASTTUBE and blue and green triangles to simulations using NAMD with pressure difference 200 and 20 bar respectively [30, 31]. The dashed line is flow enhancement rate obtained from equation (12) with $l_s^* = 62$ and $C = 3.6$.

independence from the CNT length [4]. The asymptotic value corresponds to the situation where the pressure loss is dominated by the friction losses inside the CNT.

5. Conclusion

In summary, the present study demonstrates that continuum flow models with appropriate boundary conditions can be used to accurately predict the slip enhanced flow through CNT membranes. Here we have performed finite volume simulations of the steady-state incompressible Navier–Stokes equations subject to partial-slip boundary conditions. Our results are in agreement with corresponding MD simulations and confirm the importance of pressure loss at the CNT ends. Furthermore the present simulations enable studies at several μm long CNTs and confirm the existence of an asymptotic value for the flow rate enhancement of water inside a CNT as the CNT length increases. A novel model is proposed to describe the influence of the slip length on the pressure loss at the CNT ends, which shows the existence of an optimal slip length for the pressure losses at the CNT ends. We show that the pressure loss at the CNT ends can be significantly reduced by reducing the curvature of the edges of the CNT ends.

Acknowledgments

The authors thank CD-adapco for the support at implementing the partial-slip boundary conditions into the STAR-CD simulation package. AP and MP acknowledge financial support through grants P1-0002, J1-4134, and BI-DK/11-12-002 from the Slovenian Research Agency.

References

- [1] Majumder M, Chopra N, Andrews R and Hinds B J 2005 *Nature* **438** 44
- [2] Majumder M, Chopra N and Hinds B J 2011 *ACS Nano* **5** 3867–77
- [3] Holt J K, Park H G, Wang Y, Stadermann M, Artyukhin A B, Grigoropoulos C P, Noy A and Bakajin O 2006 *Science* **312** 1034–7
- [4] Walther J H, Ritos K, Cruz-Chu E R, Megaridis C M and Koumoutsakos P 2013 *Nano Lett.* **13** 1910–3
- [5] Gravelle S, Joly L, Detcheverry F, Ybert C, Cottin-Bizonne C and Bocquet L 2013 *Proc. Natl Acad. Soc.* **110** 16367–72
- [6] Sisan T B and Lichter S 2014 *Phys. Rev. Lett.* **112** 044501
- [7] Kalra A, Garde S and Hummer G 2003 *Proc. Natl Acad. Sci. USA* **100** 10175–80
- [8] Corry B 2008 *J. Phys. Chem. B* **112** 1427–34
- [9] Kannam S K, Todd B D, Hansen J S and Daivis P J 2012 *J. Chem. Phys.* **136** 244704
- [10] Angelikopoulos P, Papadimitriou C and Koumoutsakos P 2013 *J. Phys. Chem. B* **117** 14808–16
- [11] Sisan T B and Lichter S 2011 *Microfluid. Nanofluid.* **11** 787–91
- [12] Bocquet L and Charlaix E 2010 *Chem. Soc. Rev.* **39** 1073–95
- [13] Walther J H, Praprotnik M, Kotsalis E M and Koumoutsakos P 2012 *J. Comput. Phys.* **231** 2677–81
- [14] Hansen J S, Todd B D and Daivis P J 2011 *Phys. Rev. E* **84** 016313
- [15] Kannam S K, Todd B D, Hansen J S and Daivis P J 2011 *J. Chem. Phys.* **135** 144701
- [16] Kannam S K, Todd B D, Hansen J S and Daivis P J 2012 *J. Chem. Phys.* **136** 024705
- [17] Berendsen H J C, Grigera J R and Straatsma T P 1987 *J. Chem. Phys.* **91** 6269–71
- [18] Song Y and Dai L L 2010 *Mol. Simul.* **36** 560–7
- [19] Patankar S V 1980 *Numerical Heat Transfer and Fluid Flow* (New York: Hemisphere)
- [20] CD-adapco 2012 *STAR-CD version 4.18 Documentation*
- [21] Hansen J S, Dyre J C, Daivis P J, Todd B D and Bruus H 2011 *Phys. Rev. E* **84** 036311
- [22] Hansen J S, Daivis P J, Jeppe C, Dyre B D T and Bruus H 2013 *J. Chem. Phys.* **138** 034503
- [23] Samson R A 1890 *Phil. Trans. R. Soc. A* **182** 449–518
- [24] Roscoe R 1949 *Phil. Mag.* **40** 338–51
- [25] Joly L 2011 *J. Chem. Phys.* **135** 214705
- [26] Falk K, Sedlmeier F, Joly L, Netz R R and Bocquet L 2010 *Nano Lett.* **10** 4067–73
- [27] Falk K, Sedlmeier F, Joly L, Netz R R and Bocquet L 2012 *Langmuir* **28** 14261–72
- [28] Landau L D and Lifshitz E M 1987 *Fluid Mechanics (Course of Theoretical Physics)* 2nd edn vol 6 (Portsmouth, NH: Heinemann)
- [29] Weissberg H L 1962 *Phys. Fluids* **5** 1033–6
- [30] Walther J H, Jaffe R, Halicioglu T and Koumoutsakos P 2001 *J. Phys. Chem. B* **105** 9980–7
- [31] Phillips J C, Braun R, Wang W, Gumbart J, Tajkhorshid E, Villa E, Chipot C, Skeel R D, Kalé L and Schulten K 2005 *J. Comput. Chem.* **26** 1781–802